# ShanghaiTech Mapping Robot is All You Need: Robot System for Collecting Universal Ground Vehicle Datasets

Bowen Xu O, Xiting Zhao O, Delin Feng, Yuanyuan Yang, and Sören Schwertfeger O Senior Member, IEEE

Abstract—This paper presents the ShanghaiTech Mapping Robot, a state-of-the-art unmanned ground vehicle (UGV) designed for collecting comprehensive multi-sensor datasets to support research in robotics, computer vision, and autonomous driving. The robot is equipped with a wide array of sensors including RGB cameras, RGB-D cameras, event-based cameras, IR cameras, LiDARs, mmWave radars, IMUs, ultrasonic range finders, and a GNSS RTK receiver. The sensor suite is integrated onto a specially designed mechanical structure with a centralized power system and a synchronization mechanism to ensure spatial and temporal alignment of the sensor data. A 16-node on-board computing cluster handles sensor control, data collection, and storage. We describe the hardware and software architecture of the robot in detail and discuss the calibration procedures for the various sensors. The capabilities of the platform are demonstrated through an extensive dataset collected in diverse real-world environments. To facilitate research, we make the dataset publicly available along with the associated robot sensor calibration data. Performance evaluations on a set of standard perception and localization tasks showcase the potential of the dataset to support developments in Robot Autonomy.

Index Terms-Robotics, Computing, Cluster, Sensor Data

## I. INTRODUCTION

Localization is an essential task of all mobile robots - they need to know their pose for path planning and navigation, as well as to perform their actual task. While there exist localization methods that use external infrastructure, such as GPS or special indoor markers [1], the most general and flexible way of localization is to localize in a map [2]. Additionally, maps themselves are also needed for path planning and navigation. Thus, mapping is also a very important task for many mobile robotic systems. Typically, we need to solve those two problems together, because localization needs the map and mapping needs localization, with algorithms called Simultaneous Localization and Mapping (SLAM) [3]. Being such an essential algorithm, there is lots of research on SLAM. For proper scientific evaluation of the performance of

This work was supported by the Science and Technology Commission of Shanghai Municipality (STCSM), project 22JC1410700 "Evaluation of real-time localization and mapping algorithms for intelligent robots". This work has also been partially funded by the Shanghai Frontiers Science Center of Human-centered Artificial Intelligence.

The authors are with School of Information Science and Technology, ShanghaiTech University, Shanghai 201210, China and also with the MoE Key Laboratory of Intelligent Perception and Human-Machine Collaboration (ShanghaiTech University), Shanghai 201210, China (email: xubw@shanghaitech.edu.cn zhaoxt@shanghaitech.edu.cn fengdl@shanghaitech.edu.cn yangyy2@shanghaitech.edu.cn soerensch@shanghaitech.edu.cn).



Fig. 1. The ShanghaiTech Mapping Robot

SLAM algorithms, authors need to compare their solution to other, state-of-the-art approaches. For that, datasets of recorded robotic sensor data are used and then we typically compare the ground truth robot poses of these datasets with the poses estimated by the SLAM algorithms.

One major problem with this approach is, that there are various SLAM methods that use a multitude of different sensors and combination thereof, e.g. LiDAR, monocular camera, stereo, depth camera, event camera, radar, ultrasound, with or without IMU or odometry data. Those sensors may also be pointed in different directions or feature different resolutions or frame rates. In order to test and compare their solutions, SLAM researchers need to choose datasets compatible with their approach. But that means, that they can only compare their algorithm with other methods that work with similar datasets. Often researchers even need to collect their own dataset, suitable for their SLAM approach. The consequence of all this is, that currently, most SLAM papers only compare to a very limited number of other state-of-the-art algorithms, and it is thus often unclear how well their solution performs compared to many other, state of the art methods.

So ideally, there should be a dataset that can be used by all SLAM algorithms. Such a dataset would feature all kinds of different sensors in many different configurations, with very high specifications (e.g. resolution and frame-rate), such that SLAM algorithms can pick and choose which sensors they want, while potentially sub-sampling the data to fit their need. It is also not sufficient to do recording sessions with the different sensors in the same environment - what is needed

for proper fair, repeatable and reproducible evaluation of the algorithms is, that all sensors should follow the exact same trajectory. To collect such a dataset we thus need a robot that can collect all this different sensor data in one go. In this paper we present our efforts to build such a robot: The ShanghaiTech Mapping Robot, which is all the mapping robot needed for ground vehicle dataset collection.

The requirements for this dataset collection system are as follows: It should be a system for indoor and outdoor environments and as compact as possible. Because many sensors should be supported, which are in total quite heavy, flying systems, legged as well as hand-held solutions are impossible, so a wheeled mobile robotics base has to be chosen. While still being reasonable in terms of size, weight and consumption of power and computation resources, the robot should feature 1) as many different types sensors as possible with 2) as high specifications as possible and 3) with as big fields of view as possible. The ShanghaiTech Mapping Robot thus features 36 sensors of 9 different modalities. The amount of data collected by all of these sensors can be up to 3,000 MiB per second. To facilitate the collection and storage of all this data we equipped our robot with a 16-node cluster. The robot is depicted in Fig. 1.

This work was inspired by our first mapping dataset collection robot, which was much simpler and featured far fewer sensors [4]. In [5] we already reported on the design, construction and experiments of the 16-node "Cluster on Wheels". The ultimate goal of this work is to collect datasets that can be utilized by the SLAM Hive Benchmarking Suite [6], [7] to properly evaluate SLAM algorithms by performing 10s of thousands mapping runs and analyzing their results in-depth.

The core contributions of this paper are:

- In-depth discussion of the requirements, design and construction of the ultimate dataset collection robot;
  - Mechanical Design
  - Electrical System
  - Sensor Setup
  - Computing System
  - Distributed Software System
  - Hardware-Synchronization
- Calibration approach, esp. extrinsic calibration of 32 sensors
- Sensor Interference Evaluation
- Outdoor Dataset with SLAM Experiments

The rest of this paper is organized as follows: Section II reviews related work on SLAM datasets and multi-sensor robotic platforms. Section III describes the sensors of our data collection system, while section IV discusses the basic backbone systems of the robot and section V introduces the hardware and software integration of the sensors with the cluster as well as the hardware synchronization system. The intrinsic and extrinsic calibration procedures of the sensors are explained in section VI. Section VII then reports on the data collection and post-processing procedures. A few sensors interfere with each other and the limited effect of this is investigated and described in section VIII. The outdoor dataset provided with the paper, as well as SLAM experiments with it,

are presented in section IX. This paper concludes with section X, also discussing the future work. Details of the data collected by the robot are provided in Appendix A.

#### II. RELATED WORKS

The development of acquisition of SLAM datasets has been crucial for advancing research in robotics, computer vision, and autonomous driving. This section reviews relevant datasets and techniques, focusing on multi-sensor approaches, visual SLAM, LiDAR-based systems, event-based cameras, and mmWave radar applications.

Several large-scale datasets have been instrumental in driving progress in autonomous vehicle research. The KITTI dataset [8], introduced in 2013, was one of the pioneering efforts, providing synchronized stereo imagery, LiDAR scans, and GPS/IMU data. Building upon this foundation, the Oxford RobotCar dataset [9] offered long-term data collection over varying conditions, while the Cityscapes dataset [10] focused on semantic understanding of urban scenes. More recent contributions like nuScenes [11] and Waymo Open Dataset [12] have further expanded the scope, incorporating additional sensor modalities and more diverse driving scenarios. The Ford Multi-AV Seasonal Dataset [13] specifically addresses the challenges of seasonal variations. Our work distinguishes itself from these datasets by offering a more extensive and diverse sensor suite, including event-based cameras, infra-red cameras, a combination of 5 different LiDARs models, and a multidirectional mmWave radars setup, which are not commonly found in existing datasets.

LiDAR approaches are one of the prevalent SLAM methods, as well as for 3D reconstruction and autonomous driving applications. Datasets such as M2DGR [14] and the Multi-Modal Lidar Dataset [15] have provided valuable resources for developing and evaluating LiDAR-based SLAM algorithms. The RUGD dataset [16] specifically targets unstructured environments, while PandaSet [17] offers a comprehensive sensor suite including LiDAR for autonomous driving research. Our work builds upon these efforts by integrating high-resolution LiDAR data with other sensor modalities, allowing for more robust and versatile perception algorithms.

Visual SLAM, as yet another key approach of SLAM, has seen significant advancements, fundamentally owing to the availability of diverse datasets. The EuRoC MAV datasets [18] provided benchmark data for aerial vehicles, while more recent works like the multi-camera framework by Kaveti et al. [19] and the visual-inertial odometry system by Zhang et al. [20] have explored multi-camera setups for improved robustness. The Campus Map dataset [21] offers a large-scale multi-camera dataset with additional sensors, similar to our approach. However, our work extends beyond this by incorporating event-based cameras and mmWave radars, enabling research into fusion algorithms that can leverage these novel sensing modalities.

Event-based cameras have emerged as a promising technology for high-speed and high-dynamic-range applications. Datasets such as ViViD++ [22], DSEC [23], and VECtor [24] have provided valuable resources for developing event-based SLAM and odometry algorithms. The Event-Camera

Dataset and Simulator [25] and the Multivehicle Stereo Event Camera Dataset [26] have further expanded the available data for event-based research. Our work incorporates event-based cameras alongside traditional sensors. It allows for the development of hybrid algorithms like [27] that can exploit the complementary strengths of different sensor modalities while also creates a benchmark for various event-based algorithms to compete with their visual or lidar-based counterparts.

The use of mmWave radar in SLAM and autonomous driving is an emerging field with significant potential. Recent works such as the multi-radar inertial odometry by Huang et al. [28] and the 4D imaging radar inertial odometry and mapping (iRIOM) by Zhuang et al. [29] have demonstrated the capabilities of mmWave radar for ego-motion estimation and mapping. Park et al. [30] proposed a novel radar velocity factor for pose-graph SLAM, while Lu et al. [31] developed milliMap for robust indoor mapping using mmWave radar. Our robot includes mmWave radar data, enabling research into multi-sensor fusion algorithms that can leverage the unique properties of radar, such as detecting glass, using the Doppler effect to meature object's speed and its robustness in adverse weather conditions.

In summary, while existing datasets have made significant contributions to various aspects of SLAM and autonomous driving research, our work uniquely combines a wide array of sensor modalities, including event-based cameras and mmWave radars. This comprehensive approach allows for the development and evaluation of more robust and versatile algorithms capable of operating in diverse and challenging environments.

#### III. SENSOR SUITE

Ground vehicles like road automotive, warehouse AGVs, or even household robot vacuum cleaners, all have different sensors equipped, suiting their size, environment of operation and budget. Moreover, the choice of sensor is affected by the indented mission of the vehicle. Most vehicles would use the data for basic localization and mapping, while some of them also expect fine reconstruction of environment or detecting surrounding objects they try to avoid bumping into (or contrarily, would like to interact with).

Different types of sensors suit different tasks. To achieve the goal of collecting universal ground vehicle datasets, we tried our best to equip our robot with almost all kinds of sensors utilized in SLAM and self-driving field, hoping that the datasets it produce would fit most, if not all, SLAM algorithms. To be specific, our choice covers visual sensors (including frame-based RGB cameras, depth cameras, infrared cameras and event-based cameras), LiDARs (including rotational ones and solid ones), inertial sensors, mmWave radars, ultrasonic range finders and GNSS receivers. In this section, we will introduce the sensor suite on the robot.

## A. RGB Cameras

Color cameras are some of the most used sensors in the SLAM field, providing data for visual SLAM algorithms, as well as providing input for advanced computer vision algorithms like semantic segmentation or object detection. Conventional algorithms such as ORB-SLAM3 utilize either monocular or stereo visual streams [32].

Bird's-Eye-View data, stitched from omni-directional cameras, is also very popular recently, e.g. [33].

Thus we equipped the mapping robot with 2 models of RGB cameras, FLIR Grasshopper3 (GS3-U3-51S5C-C) and FLIR LadyBug5+.

FLIR Grasshopper3 (GS3-U3-51S5C-C) (Fig. 2-b) is a 2/3-inch color camera that has a resolution of  $2448 \times 2048$  pixel (5MP) and can capture images in global shutter mode at the frame rate up to 75fps. [34] Our initiative was to use them to achieve stereo view towards five main directions: front, back, left, right, up, and to have a monocular downward view of the floor or ground the robot drives on. FLIR LadyBug5+ (Fig. 2-a) is a polydioptric omnidirectional color camera, consisting of 6 pinhole cameras. 5 of the cameras face the surrounding while the last one faces upward. Each of the 6 sensors has a resolution of  $2464 \times 2048$  and a maximum frame rate of 30fps [35].

## B. RGB-Depth Cameras

Compared to RGB camera that provides no depth measurement, RGB-Depth camera captures both color (RGB) and depth information simultaneously. It combines a standard color camera with a depth sensor, providing a 3D representation of the captured scene.

We chose Azure Kinect DK (Fig. 2-c) as the RGB-D camera of our robot. It features a 12MP high-resolution ( $3072 \times 1920$ ) RGB camera that can capture color images in global shutter mode at 30fps and an 1MP depth camera that uses ToF technology to measure distance within the range of 0.5 - 5.46 meters [36]. Compared to depth cameras that use structured light technology, ToF RGB-D cameras work better in outdoor environments and have a longer range, which is more suitable for our robot.

We wanted our robot to have multiple Azure Kinect DKs, respectively cover the front, back, left, right, and up direction.

## C. IR Cameras

IR cameras can measure temperature and thus be used to tell heat-emitting objects like human beings, animals, vehicles, etc., from the background. They are also good at detecting fire or malfunctioning electricity equipment.

For our robot, we chose FLIR A315 (Fig. 2-e) , a compact uncooled microbolometer thermal camera. A315 features a  $320 \times 240$  pixels Vanadium Oxide detector, having a temperature detection range from -20°C to 120°C with an accuracy up to  $\pm 2$ °C. Its built-in lens provides a 25° field of view and motorized focusing control. It has a spatial resolution of 1.36 mrad and a temperature resolution of 50 mK. Two A315s should be used to form a forward looking stereo pair.

## D. Event-based Cameras

Unlike conventional frame-based cameras, event-based cameras capture asynchronous 'Contrast Detector' events representing per-pixel brightness changes and report them at real-time, instead of reading out full frames at a fixed rate, which



Fig. 2. Sensors on ShanghaiTech Mapping Robot.

 $\begin{tabular}{l} TABLE\ I\\ SENSOR\ CONFIGURATION\ OF\ THE\ SHANGHAITECH\ MAPPING\ ROBOT\\ \end{tabular}$ 

Sensor Type	Model	Qty	Specifications	Max Data Rate	Field of View	Looking Direction	Appearance
RGB Camera	FLIR Grasshopper3	11	2448 x 2048 pixels	75 fps	81.9° x 61.2°	Front, Back, Left, Right, Up (stereo); Down (mono)	Fig. 2-b
RGB Camera	FLIR LadyBug5+	1 (6)	6 x 2464 x 2048 pixels	30 fps	90% of full sphere	Omnidirectional	Fig. 2-a
RGB-D Camera	Azure Kinect DK	5	RGB: 3072 x 1920, Depth: 1MP	30 fps	N/A	Front, Back, Left, Right, Up	Fig. 2-c
IR Camera	FLIR A315	2	320 x 240 pixels	60 Hz	25°	Front (stereo pair)	Fig. 2-e
Event-based Camera	EvC3A	2	640 x 480 pixels	N/A	N/A	Front (stereo pair)	Fig. 2-d
Spinning LiDAR	Robosense Ruby	2	128 beams, 200m range	10 Hz	360° x 40°	Horizontal, Vertical (90° pitched)	Fig. 2-i
Spinning LiDAR	Hesai PandarQT	1	64 beams, 60m range	10 Hz	360° x 104.2°	Horizontal	Fig. 2-h
Spinning LiDAR	Robosense Bpearl	2	32 beams, 30m range	10 Hz	360° x 90°	Front, Back	Fig. 2-j
Solid-state LiDAR	Livox Avia	1	190m range	10 Hz	70.4° x 77.2°	Front	Fig. 2-k
Solid-state LiDAR	Neuvition M1	1	200m range	10 Hz	45° x 25°	Front	Fig. 2-1
IMU	Xsens MTi-630R	1	400 Hz update rate	400 Hz	N/A	N/A	Fig. 2-g
Ultrasonic Sensor	KS103 bundle	1	1cm to 8m range	N/A	13 different angles	Front	Fig. 2-m
mmWave Radar	TI IWR6843AOPEVM	5	60GHz	N/A	120° x 120°	Front, Back, Left, Right, Up	Fig. 2-n
GNSS Receiver	Bynav A1	1	Dual antenna with IMU	N/A	N/A	N/A	Fig. 2-f
	Total 36 (41) 17 RCR 5 RCR-D 2 Event-based 2 IR 7 LiDARs 5 mmWaye Radars 1 Sonar Set 1 IMU 1 CNSS RTK/INS						

means that event-based cameras can distinguish motion at a very high speed rate, introducing a new approach into the field of visual SLAM.

We equipped the robot with EvC3A event-based cameras (Fig. 2-d) featuring the Prophesee PPS3MVCD sensor (often being referred as the Gen3.1 VGA Sensor) also used in the EVK3 camera [37]. It has a resolution of  $640 \times 480$  on its 3/4" sensor, achieving a typical latency of  $200\mu s$  and a dynamic range above 120dB. Two of them should be deployed to form a forward looking stereo pair.

## E. LiDARs

LiDAR-based approaches have always, along with their visual counterparts, sat in the center of the field of SLAM. Featuring straightforward capability in range measuring, LiDARs appear on the whole spectrum of ground vehicles, from

\$500 robot vacuum cleaners to \$50,000 road automotive. To produce a universal ground vehicle dataset, LiDARs, many of them, are a must.

In order to diversify the technical methodologies employed by the LiDAR systems and facilitate comprehensive coverage of the sensing area in all directions, we equipped the robot with seven LiDARs, encompassing five distinct models: Robosense Ruby , Robosense Bpearl , Hesai PandarQT , Livox Avia, and Neuvition M1.

Robosense Ruby and Hesai PandarQT are conventional rotational LiDARs. Robosense Ruby (Fig. 2-i) is a 128-beam LiDAR with a 0.1° angular resolution on both the horizontal and vertical axes, 200m range and 40° vertical field of view, well-suited for autonomous driving applications requiring far detection range. In contrary, Hesai PandarQT (Fig. 2-h), also known as QT64, is a 64-beam LiDAR designed for indoor

applications. It features a 60m range, 0.6° horizontal angular resolution and has a vertical angular resolution up to 1.45°. With a 104.2° (-52.1° to +52.1°) vertical aperture, its FOV covers a typical room from the ceiling to the floor. Both of them, as well as all other LiDARs equipped by our robot, run in dual-return or triple-return mode, which can improve reflection detection accuracy [38].

Robosense Bpearl (Fig. 2-j) is a 32-beam rotational LiDAR featuring a hemispherical  $360^{\circ} \times 90^{\circ}$  field of view. It has a small blind range of less than 0.1m and a maximum range of 30m, designed for near-field detection. It provides a vertical resolution of  $2.81^{\circ}$  and a horizontal resolution up to  $0.2^{\circ}$ .

Livox Avia and Neuvition M1 are unconventional LiDARs. Livox Avia (Fig. 2-k) is a semi-solid-state LiDAR featuring a unique non-repetitive scanning pattern and a forward-looking field of view. Unlike conventional rotational LiDARs, Livox Avia's coverage area ratio increases with the time of integration. It has a  $70.4^{\circ} \times 77.2^{\circ}$  field of view, 190m range and  $\pm 2$ cm accuracy. It features a best point density among all 5 LiDARs euipped by our robot and thus fits use cases like fine mapping and 3D reconstruction. Neuvition M1 (Fig. 2-l) is a MEMS-based solid-state lidar, providing a  $45^{\circ} \times 25^{\circ}$  field of view with a  $1750 \times 480$  resolution and 200m range at 20% reflectivity.

#### F. IMUs

Inertial sensors do not rely on signal returned from objects and thus are most environment-adaptive among all kinds of sensors (, geomagnetic and gravitational field do help but are not necessity, let along they are stable at most places on Earth). They can either be used alone for dead reckoning or work with cameras, LiDARs or GNSS receiver to perform multi-sensor fusion localization.

We chose MTi-630R (Fig. 2-g), a rugged and compact attitude and heading reference system (AHRS) from Xsens, to be the main IMU of our robot. It provides 0.2° RMS roll/pitch and 1° RMS heading accuracy and is able to perform high precision strapdown integration at 400Hz [39]. It also measures temperature and atmospheric pressure, potentially helps determine the elevation of robot indoor.

Devices like Livox Avia, Azure Kinect DKs, and the GNSS receiver also have their own built-in IMU.

#### G. Ultrasound Range Finders

Ultrasound Range Finders are often equipped by road vehicles for detecting near-field obstacles especially in the context of automatic parking. We equipped our robot with 13 KS103 ultrasonic range finders (Fig. 2-m) . KS103 has a range of 1cm to 8m and a resolution of 1cm. It utilizes proprietary filtering techniques to improve ranging accuracy, claiming high precision even in noisy environments.

## H. mmWave Radars

mmWave Radar is yet another type of sensors that often appears on road vehicles. They can robustly detect the position and relative speed of objects like pedestrians, cyclists, and other vehicles, thus often used to provide functions like Blind Spot Detection and Autonomous Emergency Braking.

For our robot, we chose IWR6843AOPEVM (Fig. 2-n), a 60GHz mmWave radar from TI. It achieves a wide 120° azimuth and 120° elevation field of view with a small antenna-on-package module [40]. We decided to have five of these radars to look at front, back, left, right, and up directions.

#### I. GNSS receiver

To measure an accurate trajectory serving as ground truth in outdoor use cases, GNSS is the best choice. With the assistance of differential reference stations, onboard IMU, and some magic of post-mission processing, GNSS receivers can achieve an accuracy up to 1cm.

We employed a Bynav A1 GNSS RTK receiver (Fig. 2-f) that utilizes GPS, GLONASS, Galileo, BeiDou, QZSS, and NAVIC constellations. The receiver supports dual antenna setup, measuring not only the position but also the attitude of the robot. It also has an builtin INS that helps improve positioning both in real-time and for processing afterwards.

#### IV. SYSTEM BACKBONE

To make all the sensors mentioned above work simultaneously on our robot, proper data communication, synchronization, powering, as well as an moving base is essential. In this section, we will introduce several main pieces of system hardware acting as the backbone infrastructure of sensing.

## A. Husky UGV

Our robot is built upon Clearpath Husky, a 990mm long, 670mm wide UGV equipped with rugged construction, high-torque differential drive and lug-tread tires. It has full terrain mobility that allow us to collect datasets in a whole span of various environments, from the interior of buildings, paved roads, to grass fields or even forests.



Fig. 3. The Clearpath Husky UGV.

## B. Computation Cluster

To control all the sensors and record the data captured by them, a powerful computer is essential for our mapping robot. [5] Since there are too many sensors on the mapping robot while each of them could capture massive amount of data, even the most powerful portable computer does not have enough I/O and storage bandwidth to handle the recording of data from all sensors. A 16-node computation cluster is specially designed for this usage.

The cluster consists of 16 computing nodes, each modified from an ASUS Mini PN51 computer, having a 8-core, 16-threads Ryzen 7 5700U processor, 32 GiB of RAM, 2 TiB of NVME M.2 SSD storage (Samsung 970EVO Plus, sequential write speed up to 3,300 MB/s), 2 Gigabit Ethernet cards, 3 USB 3.2 Gen1 Type-A ports and 2 USB 3.2 Gen2 Type-C ports. The nodes are stacked in a customized case which also accommodates several DC-DC converters and a LAN switch providing power and interconnection for the cluster, as showed in Fig. 4.



Fig. 4. The 16 nodes of the cluster (left) and the complete cluster without one side wall (right).

Among the nodes there is one master node that acts as the controller of the whole cluster while the other worker nodes do not have their operating system install locally but utilize network boot and use the system image hosted on the master node, making it much easier to configure the sensor drivers and orchestration programs over all 16 nodes. This approach also saves storage on worker nodes, allowing a longer record time.

Each worker node is intended to control and record up to 4 sensors, including 3 through USB 3.0 connection and one through Gigabit Ethernet connection. Sensor drivers help configure the sensors connected to the according node and collect the captured data. Raw sensor data will be saved in situ to the SSD mounted on the worker node and can, on demand, be streamed to the master node through ROS. Recorded sensor data can be collected for post-processing by either copying them to external hard drives connected to worker nodes or forwarding them through the master node to an external server.

## C. Synchronization Board

To eliminate or remedy the time difference of data collected by different sensors, either electronic synchronization or IEEE 1588 PTP (Precision Time Protocol) is the most preferred approach. Both of them can achieve sub-microsecond precision. We employed Syncboard, a combination of Raspberry Pi 4 computer and specially designed I/O shield, to act as a master clock of the whole robot that provides triggering or time base for sensors equipped as well as computation nodes in the cluster. On the Syncboard there are 12 triggering output channels and a LiDAR synchronization channel, capable of connecting at most 130 sensors.

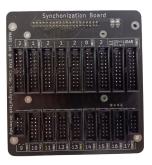




Fig. 5. The front side of Syncboard (left). Syncboard installed on the cluster and plugged with triggering cables of sensors (right).

Each of the 12 triggering output channels can generate square wave signals according to the channel-wise designated parameters including frequency (up to 1000Hz), triggering edge polarity (rising edge, failing edge or both edges), time offset and duty ratio, adapting to various triggering-compatible sensors like cameras and IMU. Voltage level of each channel can be set to 3.3V or 5V by changing the soldering bridge on the board. One channel may have 6 to 40 vacancies available for sensor connection, enabling us to easily trigger multiple sensors with the same signal.

The LiDAR synchronization channel, on the other hand, is capable of generating GPRMC+PPS signal. GPRMC, or the Recommended Minimum Specific GPS/Transit Data, is an NMEA 0183 message type designed for carrying positioning data, including a timestamp accurate to the second. It is often given along with a PPS (Pulse-per-Second) signal that indicates the exact beginning of the second contained in the message. Conventional LiDARs consume GPRMC+PPS signal, often from a real GPS receiver in old days, to set their internal clock. The channel can be configured to have certain baud rate as well as an original or inverted voltage level to adapt to different LiDARs. The channel provides 10 vacencies for LiDAR connection.

Nevertheless, Syncboard broadcasts its clock using PTP throughout the cluster LAN such that all computing nodes can synchronize themselves as well as the sensors connected to them. Syncboard itself takes either GNSS or public NTP server as its external master clock.

Syncboard also provides a handy LED button for us to physically start or stop triggering and check its working status, no need to send commands on remote devices.

#### D. Power Box

We designed a power box to provide electricity to all sensors of various types as well as the computation cluster and the UGV base. The power box is able to get power from lithium batteries, convert them into different voltage rails and distributes them to all electric devices.

The power box is equipped with 2 independent battery connectors. High current diodes are employed to isolate the two inputs, enabling the hot swap of batteries and preventing them from charging each other. After flowing through the diodes, electricity meets the main breaker which protects the robot from over-current and acts as the power switch of the

robot, then a digital power meter which displays the realtime voltage, current, power, and an integration of energy consumption, before being distributed into converters.

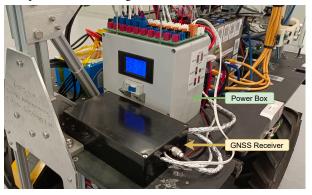


Fig. 6. The power box and GNSS receiver of ShanghaiTech Mapping Robot Inside the power box, multiple DC-DC converters turn the battery power rail into 4 stable DC rails, 5V, 12V, 19V, 24V respectively. The 4 converted rails along side with the battery power rail are connected to the power distribution board, showed in Fig. 7, at the top of the power box. Sensors get electricity from sockets on this board unless they use a single USB port for both data and powering. In that case, they get power from cluster nodes. The UGV base and the computation cluster have their power line connected to the back of the power box to get battery power rail directly.

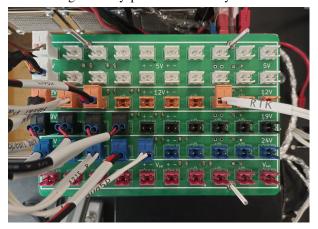


Fig. 7. The distribution board at the top of power box. Power lines of several sensors are connected to the box to get electricity of different voltage.

#### V. System Integration & Sensor Setup

With all sensors and backbone hardware ready, in this section we will introduce how we integrated all components together as well as the setup of each sensor. As showed in Fig. 8, we designed a sensor deck, a front sensor tower and a back sensor tower to accommodate all sensors

#### A. Front Sensor Tower

The front sensor tower consists of multiple floors, each of them is made of either aluminum or plastic boards.

On the top there mounts the front GNSS antenna as well as 2 rotational LiDARs, Hesai PandarQT and the first (front) Robosense Ruby.

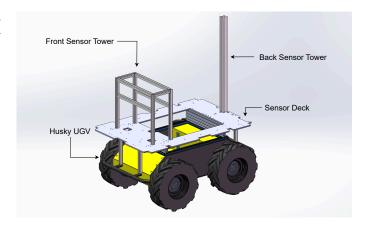


Fig. 8. A simplified model of ShanghaiTech Mapping Robot 's mechanical design, showing Clearpath Husky UGV, the sensor deck, front sensor tower and back sensor tower.

As showed in Fig. 10 and Fig. 15, PandarQT deserves a position on the very top to observe robot's near surrounding, including objects at very low angle, with no obstruction. Stayed straight under PandarQT, the front Ruby covers far away objects. Both LiDARs, as well as all rest of them, are connected to separate cluster nodes through Ethernet cable. Each of these nodes handles the control and data acquisition of the respective LiDAR. Robosense LiDARs are synced using the LiDAR synchronization channel mentioned in Sec. IV-C while LiDARs of other models use PTP protocol to get time base from the syncboard relayed by the cluster nodes.

One floor lower, the first (front) Robosense Bpearl is installed on the front panel. Its zenith of the FoV points forward, providing a hemispherical view of the front of the robot, also showed in Fig. 15.

Behind the front Bpearl, 2 Grasshopper3 cameras, one Azure Kinect DK and a mmWave Radar, showed in Fig. 10 and Fig. 9 are attached on the two side panels and the back panel of this floor. They look upwards and provide a view of ceilings or treetop above. Inside this floor, there stashes the cables and I/O boxes of all LiDARs on the robot.

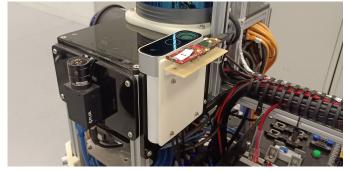


Fig. 9. The upward looking Azure Kinect DK and TI IWR6843AOPEVM mmWave radar.

These 2 up-looking Grasshopper3 cameras, as well as their front-, left-, right- and back-looking counterparts, are equipped with Kowa LM6JC wide-angle lenses. It has a focal length of 6mm, providing a wide FoV of  $81.9^{\circ} \times 61.2^{\circ}$  and a deep depth of view. [41] We set the focal distance to  $\infty$  and aperture to their maximum value of f/1.4 to ensure a sharp imaging on far surrounding objects and let sufficient amount of light reach the

sensors, enabling high frame-rate capturing. These 10 cameras run in hardware triggering mode and are connected to the same triggering channel on the Syncboard, thus capture images at the same time, with same frame rate.

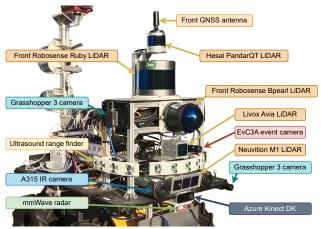


Fig. 10. The front sensor tower of ShanghaiTech Mapping Robot.

Another floor lower, there are 2 EvC3A event-based cameras, MTi-630R IMU, Livox Avia LiDAR, and 13 KS103 ultrasound range finders. The 2 EvC3A event-based cameras form a stereo pair looking forward, using same lenses as Grasshopper3's. The focal distance setting is of the same but the aperture is set to the smallest since event-based sensors capture the change of brightness instead of the absolute brightness and work better with reasonably limited lighting. The 2 event-cameras synchronize their internal clock with each other using a 1 MHz signal and also receive triggering signals from Syncboard. However, instead of following triggering signals to capture whole frames as frame-based cameras would do, event-based cameras percept them as 'External Trigger' events which would be stored in the same stream along with 'Contrast Detector' events mentioned in Sec. III-D.

MTi-630R is configured to measure linear acceleration, angular velocity, orientation as well as magnetic heading, atmospheric pressure and temperature, all at a rate of up to 400Hz triggered by Syncboard. KS103 ultrasound range finders are installed on curved racks attached to the tower to achieve evenly angled detecting directions. All 13 of them are connected via an I<sup>2</sup>C bus to a microcontroller which triggers them in an interleaved sequence to avoid cross-talk.

At the bottom of front sensor tower, 2 A315 IR cameras and the Neuvition M1 LiDAR are mounted on the front end of the sensor deck. A315 is equipped with a 18mm lens providing a 25° FoV and has motorized focus motor enabling automatic focusing control. We configured them to output a 16-bit linear temperature image at a frame rate of 60 Hz. They are connected over a Gigabit Ethernet connection to designated cluster nodes that handle their recording and controlling.

At the front of the UGV base, there is a downward looking Grasshopper3 camera, as showed in Fig. 11. Its focal distance is set to match the distance to the ground in order to get a clear view of the floor, road, etc. Alongside it, two 1.5-watt LED lights are installed to ensure enough lighting, enabling a even higher frame rate to compensate for the limited FoV (about  $40 \times 60$  cm on the ground) due to its low mounting

position. We dedicated a triggering channel of Syncboard for this camera to drive it at a different, often faster, frame rate than its counterparts looking around and upward.



Fig. 11. The downward looking Grasshopper3 and LED lights.

#### B. Sensor Deck

The sensor deck is made out of one aluminum plate and forms the length and width of the vehicle. It's mounted directly onto the base UGV by being bolted to the main aluminum extrusion frame around the top of UGV's payload bay and further supported by aluminum pillars attached to the front and rear bumper bars. Both the front and back sensor tower are attached to the sensor deck. The computation cluster, power box and one out of the 2 batteries are placed through a slot of sensor deck, marked yellow in Fig. 12, onto the UGV's payload bay.

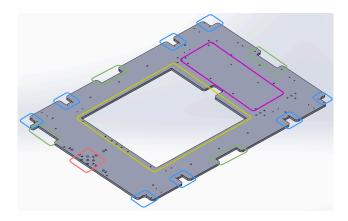


Fig. 12. The design of ShanghaiTech Mapping Robot's sensor deck. Mounting position for Grasshopper3 (blue), Azure Kinect DK (green), computation cluster (yellow), front sensor tower (purple) and back sensor tower (red).

The sensor deck accommodates the Grasshopper3 cameras, Azure Kinect DK depth cameras and the mmWave radars facing the rest 4 (front, back, left and right) directions. In each direction, the 2 separate Grasshopper3 mounting slots, marked blue in Fig. 12, are capable of aligning the direction and sensor plane of cameras, forming them into a stereo pair.

As showed in Fig. 13, each mmWave radar is mounted on the back of a Azure Kinect DK using a 3D printed part, forming a Kinect-mmWave pair. Such pairs are attached to Kinect mounting slots of sensor deck, marked green in Fig. 12. Such approach insures a uniform translation between all 5

pairs thus helps simplifying the calibration of mmWave radar extrinsics. While mmWave radars do not support hardware triggering, Azure Kinect DKs do. They are all configured to run in the subordinate mode and have their sync-in ports connected to a dedicated triggering channel of Syncboard generating VSync signal at desired frame rate.



Fig. 13. The design (right) and actual photo (left) of 3D printed part connecting Azure Kinect DK and mmWave radar.

The real-time kinematics GNSS receiver is placed on the sensor deck near the back sensor tower. Its 2 antennas are installed atop the front and back sensor tower respectively. The receiver is connected to the cluster LAN and thus has access to online differential corrections data via a 5G cellular link from either local base station or third-party CORS (Continuously Operating Reference Stations) network. It also sends PPS signal to Syncboard via a dedicated cable when acts as an external master clock as mentioned in Sec. IV-C.

The powering, data and synchronization cables of the sensors are routed on the bottom side of the deck.

#### C. Back Sensor Tower

The back sensor tower is made out of a single 40mm\*40mm aluminum extrusion pillar. Along the pillar there attaches 2 rotational LiDARs, the omnidirectional camera, the rear GNSS antenna as well as WiFi, cellular and joystick receivers.

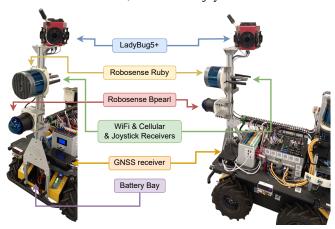


Fig. 14. The back sensor tower of ShanghaiTech Mapping Robot viewed from its back (left) and right (right).

The LadyBug5+ is mounted at the top of the back sensor tower. The built-in lenses of LadyBug5+ have a f/2.5 aperture and a 4.4mm focal length, achieving a FoV of 90% full sphere (6 sensors combined) and acceptable sharpness from about 60cm to infinity. [35] We capture original pinhole images from the 6 sensors rather than using its SDK to stitched panorama images on the fly. It is triggered via a dedicated channel of Syncboard. The back GNSS antenna is placed on the top of

LadyBug5+ in a particular orientation that hides itself in a blind spot.

At the middle of the back sensor tower there mount the second (back) Robosense Ruby and Bpearl. are installed on the robot. The back Bpearl simply points the zenith of its FoV backwards, opposite to its front counterpart, while the back Ruby is installed vertically, pitched up 90°, achieving a dense vertical scanning and coverage of far objects with high elevation angle like tall buildings along the routes. In Fig. 15, we show the FoV of all 7 LiDARs on the robot.

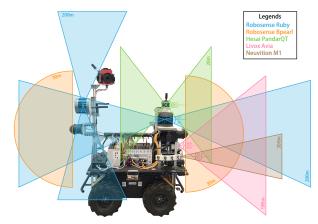


Fig. 15. FoV of LiDARs equipped by ShanghaiTech Mapping Robot.

A USB hub is installed on the back sensor tower to accommodate WiFi, cellular and joystick receivers, providing connectivity to the robot for controlling, monitoring, and access to online reference servers for time and differential GNSS.

Under the back sensor tower, a second battery is installed in the back bay of UGV.

With everything connected, the communication and synchronization architecture of the whole robot are as shown in Fig. 16 and Fig. 17

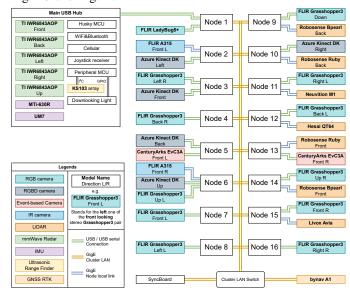


Fig. 16. The communication structure of the ShanghaiTech Mapping Robot.

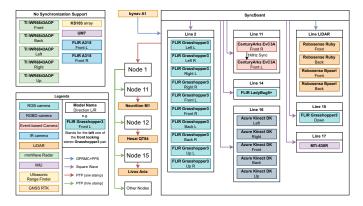


Fig. 17. The synchronization flow of the ShanghaiTech Mapping Robot.

#### VI. CALIBRATION

To ensure accurate perception and mapping, it is crucial to calibrate the intrinsic and extrinsic parameters of the various sensors employed in the system. There are various tools suitable for our use case, including ones concentrate on sensors of one same type [42], [43], [44], and others performing cross-modal calibration [45], [46], [47] and [48]. This section outlines the calibration procedures for the RGB cameras, event-based cameras, and LiDAR sensors.

## A. Camera Intrinsic & Extrinsic Calibration

The intrinsic and extrinsic parameters of 21 out of the 22 RGB cameras, including 10 Grasshopper3, 5 Azure Kinect DK, and 6 individual sensors of the LadyBug5+, were calibrated using the multi-camera calibration toolbox Kalibr [42] and AprilGrid patterns. Kalibr is capable of calibrating the intrinsic and extrinsic parameters of camera systems with non-globally shared overlapping fields of view and supports various distortion models, such as radial-tangential and equidistant models, which accurately represent the lenses used on the Grasshopper3 and the built-in fisheye lenses on the Ladybug5+, respectively.

For each of the 5 main directions (front, back, left, right, and up), the 2 Grasshopper3s, 1 Azure Kinect DK, and 1 or 2 sensors of the LadyBug5+ facing that side are grouped and calibrated together since they share a similar perspective. This gave us intrinsics of all cameras and 5 extrinsics groups, each independent from the others. Subsequently, the extrinsics between the 5 surrounding LadyBug5+ sensors were calibrated in a separate run, connecting the extrinsics of the 4 horizontal sides (front, back, left, and right). The up-looking side was finally connected to the extrinsic tree using the factory precalibrated transformation between the front-looking and up-looking sensors of the LadyBug5+.

The intrinsic parameters of the last, down-looking Grasshopper3 camera were calibrated using the ROS camera calibration package [49] and a checkerboard target with a size matching the small area of view on the ground. Considering that the camera has no overlapping field of view with any other onboard sensors and that the down-looking image stream is more likely to be used in monocular image registration algorithms rather than visual odometry algorithms, its extrinsic

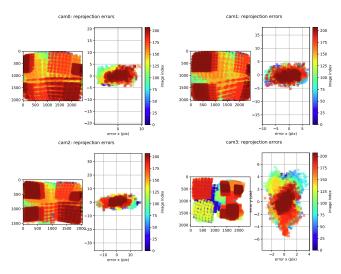


Fig. 18. Reprojection error of 4 frontward looking RGB cameras after calibration by Kalibr. (cam0: stereo left Grasshopper3, cam1: stereo right Grasshopper3, cam2: Azure Kinect DK RGB sensor, cam3: LadyBug5+ sensor number 0)

parameters were derived from the structure design instead of using complex calibration algorithms.

The intrinsic parameters of the two EvC3A event-based cameras were calibrated using blinking checkerboard patterns and the calibration tool provided by the Metavision SDK. The extrinsics of the event-cameras were calibrated using Kalibr, utilizing the frame images rendered from the two event streams along with the two image streams captured by the two front-facing Grasshopper3 cameras.

#### B. LiDAR Extrinsic Calibration

The extrinsics between the LiDARs and cameras were calibrated using a combination of LiDAR-Camera and LiDAR-LiDAR approaches. The extrinsic between the front-looking camera of the Ladybug5+ and the Livox Avia LiDAR was estimated using the direct visual-LiDAR calibration toolbox [45]. The Livox Avia's non-repetitive scanning pattern provides a dense point cloud of the scene in front of the stationary robot, which the toolbox utilizes for accurate direct pixel-level registration with the wide-angle camera image captured by the LadyBug5+.

To calibrate the extrinsics between LiDARs, we registered the scans of each LiDAR against a high-precision scan from a FARO Focus 3D scanner [50]. The LiDAR scans were captured with the robot standing still and then averaged to reduce temporal noise. The registration algorithm, Iterative Closest Point (ICP) to be specific, yields the transformations between LiDARs. Combined with the camera-LiDAR transformation, all LiDARs were connected to the extrinsics tree.

## C. Calibration of Other Sensors

The MTi-630R IMU's Allan Variance parameters, including random walk and bias instability, were calibrated using the allan\_variance\_ros tool [51]. With the IMU intrinsics, the Kalibr toolbox calibrated the extrinsic between the IMU and the 2 front-looking Grasshopper3 cameras. The mmWave radars on

each side share an identical extrinsic with the respective Azure Kinect camera they attached onto, derived from the 3D printed mount's design. The extrinsics of the ultrasound range finders and other unmentioned sensors were either roughly measured manually or derived from their mounts' structure design.

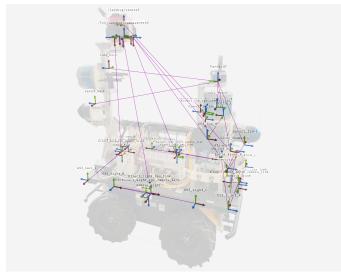


Fig. 19. Coordinates of calibrated sensors. Purple lines indicate the edges of transformation tree. An image of mapping robot took from a roughly same perspective is also shown.

#### VII. PROCEDURES AND POST-PROCESSING

The mapping robot is designed with distributed computation in mind so it is vital to orchestrate all the nodes in the computation cluster along with the sensors connected to them. In this section we would introduce the procedure of data acquisition and post-process to be performed on the collected data.

## A. Procedure of data acquisition

- 1) Material Preparation: At minimum, the robot itself, one battery, and a controlling terminal like KVM or laptop is needed for performing a acquisition run. A second battery as well as backup ones or power adaptor is recommended.
- 2) Power Up: Close the main breaker on the power box. Husky UGV, the master node of the cluster, Syncboard as well as sensors getting electricity from the power box mentioned in Sec. IV-D will be powered up. Following the boot of master node, the robot becomes maneuverable.
- 3) Cluster Bringup: The master node sets itself up as the Ethernet gateway and network file systems for Boot-from-LAN, then wakes up all the worker nodes. After they boot, we can control the nodes and access data stored in them. Network access also becomes available for nodes, Syncboard and GNSS receiver.
- 4) Time Synchronization: Syncboard gets time base from external master clock and broadcasts it over cluster LAN. We would now perform a manual verification of nodes' clock, then launch the triggering for sensor test.

- 5) Sensors Bringup: The master node orchestrates all worker nodes to launch the sensor drivers. We would manually check if all sensors work as intended. If that's not the case, sensor's parameter would be modified accordingly. After everything is confirmed to work well, the triggering is turned off await the upcoming data acquisition.
- 6) Data acquisition: Command the master node to orchestrate a distributed recording of sensor data. Turn on triggering to officially start a data acquisition run. We would now drive the robot along the data acquisition route.
- 7) End of acquisition: After the robot reaches finishing position of the route, the triggering is turned off first, followed by the data recording processes. Sensor drivers stay running and do not have to be spawned repetitively until there is no more data acquisition runs to be carried out before powering off the robot. The data collected can be copied either into external hard drives via USB port from each nodes or to a workstation or network storage device through Ethernet connection, pending for post-processing.

## B. Dataset Post-processing

- 1) Timestamp Restoration: Replace the timestamps in sensor messages captured by hardware triggered sensors (Grasshopper3 camera, MTi-630R IMU, etc.) with precise triggering time of Syncboard. Any frame drop would be discovered and evaluated at the same time.
- 2) Bayer Interleaving: LadyBug5+ on-the-fly compresses each image for the 6 camera sensors in 4 separate Bayer channels using JPEG, resulting in 24 JPEG images per one capture. We decompress and interleave them to get 6 image streams, one sensor each, in bgr8 format.
- 3) Image Compression: To provide an alternative compressed version for faster distribution of our dataset, we encode each image stream using AV1 codec [52].
- 4) Mapping Ground Truth: A FARO Focus 3D scanner is used to obtain a precise point cloud of the environment along the data acquisition route, acting as the mapping or 3D reconstruction ground truth.
- 5) Trajectory Ground Truth: For route sections where GNSS signal stays available, we will post-process the onboard differential GNSS/INS data to obtain a ground truth trajectory with a typical precision of 1cm. Other than that, we register LiDAR scans to the mapping ground truth to get pose of robot as an alternative ground truth for indoor datasets.

#### VIII. LIDAR&RGBD INTERFERENCE EVALUATION

LiDARs and RGB-Depth cameras on the mapping robot emit infra-red beams and measure the time of flight to obtain distance readings. There are concerns about potential interference between the sensors. In this experiment, we collected point clouds and depth images at a fixed position against a flat, white wall in the basement of ShanghaiTech University with each LiDAR and two RGB-Depth cameras working alone (sole runs) and together (collective run) for 10 seconds, as showed in Fig. 20.



Fig. 20. Interference experiment scene setup

## A. Precision analysis

For rotational LiDARs, the temporal mean and standard deviation of distance measurements for each beam are calculated to indicate the average measurement and precision in respective directions. The mean and standard deviation of the temporal standard deviation among all beams are then computed to indicate overall precision. For unconventional LiDARs (Livox Avia and Neuvition M1), the FOV is binned in elevation and azimuth directions, and the nearest reading in each bin of each ROS pointcloud message is used. For the Azure Kinect depth camera, statistics are performed on each pixel.

$$\overline{D_b} = \frac{1}{N_t} \sum_{t=1}^{N_t} D_{t,b}$$

$$\sigma_b = \sqrt{\frac{1}{N_t - 1} \sum_{t=1}^{N_t} (D_{t,b} - \overline{D_b})^2}$$

$$\overline{\sigma_b} = \frac{1}{N_b} \sum_{b=1}^{N_b} \sigma_b$$

$$\sigma(\sigma_b) = \sqrt{\frac{1}{N_b - 1} \sum_{t=1}^{N_b} (\sigma_b - \overline{\sigma_b})^2}$$
(1)

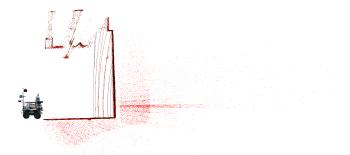
Equation 1 is used for calculating the figures for LiDAR precision analysis, where  $D_{t,b}$  is the distance measurement of beam or bin b at time t, and  $\overline{\sigma_b}$  is the mean of its temporal standard deviation.

Table II shows that all but the two Robosense Bpearls and the Livox Avia have consistent precision between the sole and collective runs, indicating that the precision of the other LiDARs is not affected by interference.

Fig. 21(a) & (b) shows the temporal mean of the point cloud collected by the front Robosense Bpearl. In the collective run, both Robosense Bpearl and Livox Avia give noisy points behind the wall or below the floor, indicating interference. However, the non-noisy points have consistent standard deviation of distance compared to the sole run, suggesting that with proper filtering, the two sensors would give point clouds of the same precision regardless of interference.

## B. Accuracy analysis

To assess the impact on accuracy, the distance between the sensors and a target plane is calculated. Significant changes in this distance would indicate interference-induced accuracy



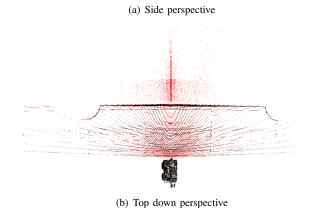


Fig. 21. (a) & (b) Average point cloud produced by front Robosense Bpearl. Black points: sole run; Red points: collective run. The robot thumbnails indicate the approximate position of the robot and do not represent the actual scale.

differences. The flat, white wall in front of the robot is used as the target plane for the 5 LiDARs on the front sensor tower, while another flat wall opposite to it is used for the back Robosense Bpearl, and the ground is used for the back Robosense Ruby.

For each sensor, point clouds from the sole and collective runs are merged separately. Points near the target plane are cropped out for accuracy evaluation. A reference plane is fitted to the selected points from the sole run, and the point-to-plane distance  $D_{c2p}$  is calculated. The Gaussian distribution of this distance is then fitted for comparison.

Table III shows that the difference in point-to-plane distance between the sole and collective runs lies within  $2\sigma$  for all LiDARs, indicating no significant accuracy change due to interference.

For depth cameras, the difference in average distance measurements between the sole and collective runs is calculated pixel-wise to detect accuracy changes. As showed in Table IV, the mean difference is much smaller than its standard deviation, indicating that the depth cameras' accuracy is also unaffected by interference.

In conclusion, among all the infra-red light-emitting Li-DARs and RGB-Depth cameras on the mapping robot, three give noisy outlier points that can be filtered out using statistical outlier removal approaches. Data from the other sensors along with the inlier data from the aforementioned three sensors have their accuracy and precision unaffected by interference. Except for the up-looking Kinect depth camera and the Hesai LiDAR, the sensors have no mutual sight, possibly preventing inescapable interference as the emitted infra-red laser does

TABLE II

MEAN & S.D. OF TEMPORAL S.D. OF DISTANCE (M)

BOLD FIGURES INDICATES SIGNIFICANT INTERFERENCE

Sensor	Sole $\overline{\sigma_b}$ (m)	Collective $\overline{\sigma_b}$ (m)	Sole $\sigma(\sigma_b)$ (m)	Collective $\sigma(\sigma_b)$ (m)
Robosense Ruby (front)	0.0165	0.0156	0.1961	0.3605
Robosense Ruby (back)	0.0104	0.0104	0.3713	0.3420
Robosense Bpearl (front)	0.0114	0.1719	0.1225	1.4642
Robosense Bpearl (back)	0.0278	0.0690	0.1970	0.8071
Hesai PandarQT	0.0367	0.0373	0.2507	0.2507
Livox Avia	0.0156	2.5236	0.0162	13.9601
Neuvition M1	0.0027	0.0028	0.0025	0.0026
Azure Kinect DK (front)	0.0775	0.1357	0.2511	0.2693
Azure Kinect DK (up)	0.2933	0.3064	0.5330	0.5361

TABLE III
MEAN & S.D. OF POINT-TO-PLANE DISTANCE (M)

Sensor	Sole $\overline{D_{c2p}}$ (m)	Collective $\overline{D_{c2p}}$ (m)	Sole $\sigma(D_{c2p})$ (m)	Collective $\sigma(D_{c2p})$ (m)	Rated Accuracy (m)
Robosense Ruby (front, strongest return)	0.0000	-0.0357	0.0219	0.0239	±0.03
Robosense Ruby (front, last return)	0.0000	-0.0020	0.0143	0.0137	±0.03
Robosense Ruby (back)	0.0000	-0.0004	0.0089	0.0088	±0.03
Robosense Bpearl (front)	0.0000	0.0022	0.0131	0.0130	±0.05
Robosense Bpearl (back)	0.0000	0.0009	0.0103	0.0078	±0.05
Hesai PandarQT	0.0000	0.0003	0.0111	0.0108	±0.03
Livox Avia	0.0000	-0.0058	0.0115	0.0115	±0.02
Neuvition M1	0.0000	-0.0029	0.0140	0.0141	±0.02

TABLE IV
PIXEL-WISE MEAN & S.D. OF DISTANCE DIFFERENCE(M)

Sensor	$\overline{D_{coll,p} - D_{sole,p}}$ (m)	$\sigma(D_{coll,p} - D_{sole,p})$ (m)		
Kinect (front)	-0.0057	0.0332		
Kinect (up)	-0.0001	0.0840		

not directly shine into the photosensitive sensors of another without reflection from a third object.

## IX. OUTDOOR DATASET

To assess the mapping robot's data acquisition capability and verify the compatibility of the collected data with SLAM algorithms, we conducted an outdoor experiment on the ShanghaiTech University campus. The experiment involved collecting data along a predefined route and running SLAM algorithms on the collected data.

## A. Data Acquisition

An 1.4 km data acquisition route, as shown in Fig. 23, was designed to include a variety of terrains and scenes on the ShanghaiTech University campus. The route was evenly split between areas around buildings and parkland, with the mapping robot primarily driving on paved roads or solid structures like bridges, and briefly on grass. Three sections of the route, surrounded by buildings, woods, or a blend of both, were revisited after traveling elsewhere, providing loop-closing opportunities for SLAM algorithms. The route also included slopes to enrich the elevation diversity.

The experiment was conducted on an overcast day, providing even lighting on objects and preventing direct sunlight



Fig. 22. Mapping robot performing data acquisition on ShanghaiTech campus

spots in the collected images. The robot took 26 minutes to traverse the entire route, ultimately collecting 2,618 GiB of data, as shown in Fig. 23. A detailed list of the recorded ROS topics is provided in the Appendix A.

## B. Lidar-based SLAM

## C. Visual SLAM

#### X. CONCLUSIONS

## XI. ACKNOWLEDGMENTS

This work was supported by Science and Technology Commission of Shanghai Municipality (STCSM), project 22JC1410700 "Evaluation of real-time localization and mapping algorithms for intelligent robots". This work has also been partially funded by the Shanghai Frontiers Science Center of Human-centered Artificial Intelligence.



Fig. 23. Ground truth trajectory of the outdoor dataset, with its start (green) and end (red) point marked out. Color of the trajectory goes from light yellow to dark orange as time progresses.

## APPENDIX A DETAILS OF ROS TOPICS RECORDED IN EXPERIMENT

In Table. V, we showed for each type and model of sensor the message topics they publish to as well as the total number of messages recorded from them. The time duration, data rate, and message type are also listed.

#### REFERENCES

- E. Olson, "Apriltag: A robust and flexible visual fiducial system," in 2011 IEEE International Conference on Robotics and Automation, 2011, pp. 3400–3407.
- [2] F. Dellaert, D. Fox, W. Burgard, and S. Thrun, "Monte carlo localization for mobile robots," in *Proceedings 1999 IEEE international conference* on robotics and automation (Cat. No. 99CH36288C), vol. 2. IEEE, 1999, pp. 1322–1328.
- [3] C. Cadena, L. Carlone, H. Carrillo, Y. Latif, D. Scaramuzza, J. Neira, I. Reid, and J. J. Leonard, "Past, present, and future of simultaneous localization and mapping: Toward the robust-perception age," *IEEE Transactions on robotics*, vol. 32, no. 6, pp. 1309–1332, 2016.
- [4] H. Chen, Z. Yang, X. Zhao, G. Weng, H. Wan, J. Luo, X. Ye, Z. Zhao, Z. He, Y. Shen et al., "Advanced mapping robot and high-resolution dataset," Robotics and Autonomous Systems, vol. 131, p. 103559, 2020.
- [5] Y. Yang, D. Feng, and S. Schwertfeger, "Cluster on wheels," in 2022 International Conference for Advancement in Technology (ICONAT), 2022, pp. 1–8.
- [6] X. Liu, Y. Yang, B. Xu, and S. Schwertfeger, "Benchmarking slam algorithms in the cloud: The slam hive system," 2024. [Online]. Available: https://arxiv.org/abs/2406.17586
- [7] Y. Yang, B. Xu, Y. Li, and S. Schwertfeger, "The slam hive benchmarking suite," in 2023 IEEE International Conference on Robotics and Automation (ICRA). IEEE, 2023, pp. 11257–11263.
- [8] A. Geiger, P. Lenz, C. Stiller, and R. Urtasun, "Vision meets robotics: The kitti dataset," *Int. J. Rob. Res.*, vol. 32, no. 11, p. 1231–1237, sep 2013. [Online]. Available: https://doi.org/10.1177/0278364913491297
- [9] W. Maddern, G. Pascoe, C. Linegar, and P. Newman, "1 year, 1000 km: The oxford robotcar dataset," *The International Journal of Robotics Research*, vol. 36, no. 1, pp. 3–15, 2017. [Online]. Available: https://doi.org/10.1177/0278364916679498
- [10] M. Cordts, M. Omran, S. Ramos, T. Rehfeld, M. Enzweiler, R. Benenson, U. Franke, S. Roth, and B. Schiele, "The cityscapes dataset for semantic urban scene understanding," in 2016 IEEE Conference on Computer Vision and Pattern Recognition (CVPR), 2016, pp. 3213–3223.
- [11] H. Caesar, V. Bankiti, A. H. Lang, S. Vora, V. E. Liong, Q. Xu, A. Krishnan, Y. Pan, G. Baldan, and O. Beijbom, "nuscenes: A multimodal dataset for autonomous driving," in 2020 IEEE/CVF Conference on Computer Vision and Pattern Recognition (CVPR), 2020, pp. 11618– 11628.

- [12] P. Sun, H. Kretzschmar, X. Dotiwalla, A. Chouard, V. Patnaik, P. Tsui, J. Guo, Y. Zhou, Y. Chai, B. Caine, V. Vasudevan, W. Han, J. Ngiam, H. Zhao, A. Timofeev, S. Ettinger, M. Krivokon, A. Gao, A. Joshi, Y. Zhang, J. Shlens, Z. Chen, and D. Anguelov, "Scalability in perception for autonomous driving: Waymo open dataset," in 2020 IEEE/CVF Conference on Computer Vision and Pattern Recognition (CVPR), 2020, pp. 2443–2451.
- [13] S. Agarwal, A. Vora, G. Pandey, W. Williams, H. Kourous, and J. McBride, "Ford multi-av seasonal dataset," *The International Journal of Robotics Research*, vol. 39, no. 12, pp. 1367–1376, 2020. [Online]. Available: https://doi.org/10.1177/0278364920961451
- [14] J. Yin, A. Li, T. Li, W. Yu, and D. Zou, "M2dgr: A multi-sensor and multi-scenario slam dataset for ground robots," *IEEE Robotics and Automation Letters*, vol. 7, no. 2, pp. 2266–2273, 2022.
- [15] L. Qingqing, Y. Xianjia, J. P. Queralta, and T. Westerlund, "Multi-modal lidar dataset for benchmarking general-purpose localization and mapping algorithms," in 2022 IEEE/RSJ International Conference on Intelligent Robots and Systems (IROS), 2022, pp. 3837–3844.
- [16] M. Wigness, S. Eum, J. G. Rogers, D. Han, and H. Kwon, "A rugd dataset for autonomous navigation and visual perception in unstructured outdoor environments," in 2019 IEEE/RSJ International Conference on Intelligent Robots and Systems (IROS), 2019, pp. 5000–5007.
- [17] P. Xiao, Z. Shao, S. Hao, Z. Zhang, X. Chai, J. Jiao, Z. Li, J. Wu, K. Sun, K. Jiang, Y. Wang, and D. Yang, "Pandaset: Advanced sensor suite dataset for autonomous driving," in 2021 IEEE International Intelligent Transportation Systems Conference (ITSC), 2021, pp. 3095–3101.
- [18] M. Burri, J. Nikolic, P. Gohl, T. Schneider, J. Rehder, S. Omari, M. W. Achtelik, and R. Siegwart, "The euroc micro aerial vehicle datasets," *The International Journal of Robotics Research*, vol. 35, no. 10, pp. 1157–1163, 2016. [Online]. Available: https://doi.org/10.1177/0278364915620033
- [19] P. Kaveti, S. N. Vaidyanathan, A. T. Chelvan, and H. Singh, "Design and evaluation of a generic visual slam framework for multi camera systems," *IEEE Robotics and Automation Letters*, vol. 8, no. 11, pp. 7368–7375, 2023.
- [20] L. Zhang, D. Wisth, M. Camurri, and M. Fallon, "Balancing the budget: Feature selection and tracking for multi-camera visual-inertial odometry," *IEEE Robotics and Automation Letters*, vol. 7, no. 2, pp. 1182–1189, 2022.
- [21] R. James, K. Nimet, M. Oscar, and B. Richard, "Campus map: A large-scale dataset to support multi-view vo, slam and bev estimation," in 2024 IEEE International Conference on Robotics and Automation (ICRA), 2024, pp. 8566–8572.
- [22] A. J. Lee, Y. Cho, Y.-s. Shin, A. Kim, and H. Myung, "Vivid++: Vision for visibility dataset," *IEEE Robotics and Automation Letters*, vol. 7, no. 3, pp. 6282–6289, 2022.
- [23] M. Gehrig, W. Aarents, D. Gehrig, and D. Scaramuzza, "Dsec: A stereo event camera dataset for driving scenarios," *IEEE Robotics and Automation Letters*, vol. 6, no. 3, pp. 4947–4954, 2021.
- [24] L. Gao, Y. Liang, J. Yang, S. Wu, C. Wang, J. Chen, and L. Kneip, "Vector: A versatile event-centric benchmark for multi-sensor slam," *IEEE Robotics and Automation Letters*, vol. 7, no. 3, pp. 8217–8224, 2022.
- [25] E. Mueggler, H. Rebecq, G. Gallego, T. Delbruck, and D. Scaramuzza, "The event-camera dataset and simulator: Event-based data for pose estimation, visual odometry, and slam," *The International Journal* of Robotics Research, vol. 36, no. 2, pp. 142–149, 2017. [Online]. Available: https://doi.org/10.1177/0278364917691115
- [26] A. Z. Zhu, D. Thakur, T. Özaslan, B. Pfrommer, V. Kumar, and K. Daniilidis, "The multivehicle stereo event camera dataset: An event camera dataset for 3d perception," *IEEE Robotics and Automation Letters*, vol. 3, no. 3, pp. 2032–2039, 2018.
- [27] A. R. Vidal, H. Rebecq, T. Horstschaefer, and D. Scaramuzza, "Ultimate slam? combining events, images, and imu for robust visual slam in hdr and high-speed scenarios," *IEEE Robotics and Automation Letters*, vol. 3, no. 2, pp. 994–1001, 2018.
- [28] J.-T. Huang, R. Xu, A. Hinduja, and M. Kaess, "Multi-radar inertial odometry for 3d state estimation using mmwave imaging radar," arXiv preprint arXiv:2311.08608, 2023.
- [29] Y. Zhuang, B. Wang, J. Huai, and M. Li, "4d iriom: 4d imaging radar inertial odometry and mapping," *IEEE Robotics and Automation Letters*, vol. 8, no. 6, pp. 3246–3253, 2023.
- [30] Y. S. Park, Y.-S. Shin, J. Kim, and A. Kim, "3d ego-motion estimation using low-cost mmwave radars via radar velocity factor for pose-graph slam," *IEEE Robotics and Automation Letters*, vol. 6, no. 4, pp. 7691– 7698, 2021.

TABLE V					
SENSOR DATA	STATISTICS	OF	OUTDOOR	DATASET	

Sensor Type	Model	Topic	Topic Count	Messages	Data Rate	Duration	Message Type
RGB Camera	FLIR Grasshopper3	/GS3_{{front,back,right,left,top}_{L,R},down}/image_raw	11	46,860	30 Hz	26:01	sensor_msgs/Image
	1	/GS3_{{front,back,right,left,top}_{L,R},down}/camera_info	11	46,860	30 Hz	26:01	sensor_msgs/CameraInfo
	FLIR LadyBug5+	/ladybug/camera{0-5}/bayer{0-3}/compressed	24	23,430	15 Hz	26:01	sensor_msgs/CompressedImage
RGB-D Camera	Azure Kinect DK	/Kinect_{front,back,right,left,top}/rgb/image_raw/compressed	5	7,989-7,992	5 Hz	26:38	sensor_msgs/CompressedImage
		/Kinect_{front,back,right,left,top}/rgb/camera_info	5	7,989-7,992	5 Hz	26:38	sensor_msgs/CameraInfo
		/Kinect_{front,back,right,left,top}/depth/image_raw	5	7,989-7,992	5 Hz	26:38	sensor_msgs/Image
		/Kinect_{front,back,right,left,top}/depth/camera_info	5	7,989-7,992	5 Hz	26:38	sensor_msgs/CameraInfo
		/Kinect_{front,back,right,left,top}/imu	5	2,651,072 (typical)	1600 Hz (typ.)	26:38	sensor_msgs/Imu
IR Camera	FLIR A315	/A315_{L,R}/image_raw	2	96,369-96,373	60 Hz	26:46	sensor_msgs/Image
Event-based Camera	EvC3A	/EvC3A_front_{L,R}/events	2	133,007-133,095	N/A	26:41	event_camera_msgs/EventPacket
Spinning LiDAR	Robosense Ruby	/ruby_{front,back}/rslidar_points	2	15,966-15,969	10 Hz	26:36	sensor_msgs/PointCloud2
	1	/ruby_{front,back}/rslidar_packets	2	19,163,367 (typ.)	N/A	26:36	rslidar_msg/RslidarPacket
	Robosense Bpearl	/bpearl_{front,back}/rslidar_points	2	15,963-15,965	10 Hz	26:36	sensor_msgs/PointCloud2
		/bpearl_{front,back}/rslidar_packets	2	4,807,801 (typ.)	N/A	26:36	rslidar_msg/RslidarPacket
	Hesai PandarQT	/hesai/pandar	1	16,031	10 Hz	26:41	sensor_msgs/PointCloud2
Solid-state LiDAR	Livox Avia	/livox/lidar	1	16,038	10 Hz	26:43	sensor_msgs/PointCloud2
		/livox/imu	1	325,608	200 Hz	26:43	sensor_msgs/Imu
	Neuvition M1	/neuvition_cloud	1	1,489	10 Hz	2:27	sensor_msgs/PointCloud2
		/neuvition_image/compressed	1	859	5 Hz	2:27	sensor_msgs/CompressedImage
IMU	Xsens MTi-630R	/mti/imu/data	1	624,797	400 Hz	26:02	sensor_msgs/Imu
		/mti/filter/free_acceleration	1	624,797	400 Hz	26:02	geometry_msgs/Vector3Stamped
		/mti/filter/quaternion	1	624,797	400 Hz	26:02	geometry_msgs/QuaternionStamped
		/mti/imu/acceleration	1	624,797	400 Hz	26:02	geometry_msgs/Vector3Stamped
		/mti/imu/angular_velocity	1	624,797	400 Hz	26:02	geometry_msgs/Vector3Stamped
		/mti/imu/dq	1	624,797	400 Hz	26:02	geometry_msgs/QuaternionStamped
		/mti/imu/dv	1	624,797	400 Hz	26:02	geometry_msgs/Vector3Stamped
		/mti/imu/mag	1	624,797	400 Hz	26:02	geometry_msgs/Vector3Stamped
		/mti/imu/time_ref	1	624,797	400 Hz	26:02	sensor_msgs/TimeReference
		/mti/pressure	1	624,797	400 Hz	26:02	sensor_msgs/FluidPressure
		/mti/temperature	1	624,797	400 Hz	26:02	sensor_msgs/Temperature
Ultrasonic Sensor	KS103	/ultrasound/range/{1-13}	13	1,387	1 Hz	26:47	sensor_msgs/Range
mmWave Radar	TI IWR6843AOPEVM	/mmWave_{front,back,left,right,top}/radar_scan_pcl	5	48,066-48,074	30 Hz	26:42	sensor_msgs/PointCloud2
		/mmWave_{front,back,left,right,top}/radar_scan	5	209,123 (typ.)	N/A	26:42	ti_mmwave_rospkg/RadarScan
GNSS Receiver	Bynav A1	/gps/fix	1	8,045	5 Hz	26:49	sensor_msgs/NavSatFix
		/gps/bestpos	1	8,045	5 Hz	26:49	novatel_gps_msgs/NovatelPosition
		/gps/bestvel	1	8,045	5 Hz	26:49	novatel_gps_msgs/NovatelVelocity
		/gps/gpgga	1	8,045	5 Hz	26:49	novatel_gps_msgs/Gpgga
		/gps/gprmc	1	8,045	5 Hz	26:49	novatel_gps_msgs/Gprmc
		/gps/gps	1	7,988	5 Hz	26:49	gps_common/GPSFix
		/gps/inspvax	1	8,046	5 Hz	26:49	novatel_gps_msgs/Inspvax
Synchronization	Syncboard	/syncboard/line/{2,14-17}	5	7,810-624,786	5-400 Hz	26:40	std_msgs/Time
	1	/syncboard/status	1	1,601	1 Hz	26:40	mars_syncboard_srvs/BoardStatus
Robot Base	Clearpath Husky	/joy_teleop/joy_selected	1	37,980	24 Hz	26:41	sensor_msgs/Joy
		/status	1	1,602	1 Hz	26:41	husky_msgs/HuskyStatus
		Total	137	# of bags: 37, size	of hags: 2.618 Gi	R	

- [31] C. X. Lu, S. Rosa, P. Zhao, B. Wang, C. Chen, J. A. Stankovic, N. Trigoni, and A. Markham, "See through smoke: robust indoor mapping with low-cost mmwave radar," in *Proceedings of the* 18th International Conference on Mobile Systems, Applications, and Services, ser. MobiSys '20. New York, NY, USA: Association for Computing Machinery, 2020, p. 14–27. [Online]. Available: https://doi.org/10.1145/3386901.3388945
- [32] C. Campos, R. Elvira, J. J. G. Rodríguez, J. M. M. Montiel, and J. D. Tardós, "Orb-slam3: An accurate open-source library for visual, visual-inertial, and multimap slam," *IEEE Transactions on Robotics*, vol. 37, no. 6, pp. 1874–1890, 2021.
- [33] Z. Li, W. Wang, H. Li, E. Xie, C. Sima, T. Lu, Y. Qiao, and J. Dai, "Bevformer: Learning bird's-eye-view representation from multi-camera images via spatiotemporal transformers," in *European conference on computer vision*. Springer, 2022, pp. 1–18.
- [34] Grasshopper3 usb3 teledyne flir. [Online]. Available: https://www.flir. com/products/grasshopper3-usb3/?model=GS3-U3-51S5C-C
- [35] Ladybug5+ teledyne flir. [Online]. Available: https://www.flir.com/ products/ladybug5plus/?model=LD5P-U3-51S5C-R
- [36] Azure kinect dk hardware specifications microsoft learn. [Online]. Available: https://learn.microsoft.com/en-us/azure/kinect-dk/hardware-specification
- [37] Silkyevcam (vga) centuryarks co., ltd. [Online]. Available: https://centuryarks.com/en/silkyevcam-vga/
- [38] X. Zhao and S. Schwertfeger, "3dref: 3d dataset and benchmark for reflection detection in rgb and lidar data," in 2024 International Conference on 3D Vision (3DV). IEEE, 2024, pp. 225–234.
- [39] Xsens mti-630r ahrs movella.com. [Online]. Available: https://www.movella.com/products/sensor-modules/xsens-mti-630r-ahrs
- [40] Iwr6843aopevm evaluation board ti.com. [Online]. Available: https://www.ti.com/tool/IWR6843AOPEVM
- [41] Kowa 2/3" lm6jc lens. [Online]. Available: https://lenses.kowa-usa.com/jc-series/479-lm6jc.html
- [42] P. Furgale, J. Rehder, and R. Siegwart, "Unified temporal and spatial calibration for multi-sensor systems," in 2013 IEEE/RSJ International Conference on Intelligent Robots and Systems, 2013, pp. 1280–1286.
- [43] I. Tahiraj, F. Fent, P. Hafemann, E. Ye, and M. Lienkamp, "Gmmcalib:

- Extrinsic calibration of lidar sensors using gmm-based joint registration," *arXiv preprint arXiv:2404.03427*, 2024.
- [44] F. Rameau, J. Park, O. Bailo, and I. S. Kweon, "Mc-calib: A generic and robust calibration toolbox for multi-camera systems," *Computer Vision and Image Understanding*, p. 103353, 2022. [Online]. Available: https://www.sciencedirect.com/science/article/pii/S1077314221001818
- [45] K. Koide, S. Oishi, M. Yokozuka, and A. Banno, "General, single-shot, target-less, and automatic lidar-camera extrinsic calibration toolbox," in 2023 IEEE International Conference on Robotics and Automation (ICRA), 2023, pp. 11301–11307.
- [46] P. Furgale, J. Rehder, and R. Siegwart, "Unified temporal and spatial calibration for multi-sensor systems," in 2013 IEEE/RSJ International Conference on Intelligent Robots and Systems, 2013, pp. 1280–1286.
- [47] X. Zhi, J. Hou, Y. Lu, L. Kneip, and S. Schwertfeger, "Multical: Spatiotemporal calibration for multiple imus, cameras and lidars," in 2022 IEEE/RSJ International Conference on Intelligent Robots and Systems (IROS). IEEE, 2022, pp. 2446–2453.
- [48] F. Zhu, Y. Ren, and F. Zhang, "Robust real-time lidar-inertial initialization," in 2022 IEEE/RSJ International Conference on Intelligent Robots and Systems (IROS). IEEE, 2022, pp. 3948–3955.
- [49] camera\_calibration ros wiki. [Online]. Available: https://wiki.ros.org/ camera\_calibration
- [50] Faro focus laser scanners. [Online]. Available: https://www.faro.com/en/Products/Hardware/Focus-Laser-Scanners
- [51] Allan variance ros. [Online]. Available: https://github.com/ori-drs/allan\_variance ros
- [52] Av1 video codec. [Online]. Available: https://aomedia.org/av1/



**Bowen Xu** received his B.S. at ShanghaiTech University in China, and now he is a second-year graduate student at ShanghaiTech University. His research focuses on Robot Mapping and SLAM.



Yuanyuan Yang received Master degree in Computer Science and Technology from ShanghaiTech University, Shanghai, China, in 2023. Her research interests include SLAM evaluation, sensor fusion and mapping for moblie robots. She is currently working.



**Prof. Dr. Sören Schwertfeger** is an Associate Professor at ShanghaiTech University, where he joined in 2014. He is the head of the Mobile Autonomous Robotics Systems Lab (MARS Lab): https://robotics.shanghaitech.edu.cn. He graduated with a Diploma (German equivalent of the Master) in Computer Science in 2005 from the University of Bremen, Germany. In 2012 he received his Ph.D. in Computer Science from the Jacobs University Bremen. Between 2012 and 2014 he was a postdoctoral researcher at the Robotics Group of Prof. Andreas

Birk at the Jacobs University Bremen. In 2010 Dr. Schwertfeger was a guest researcher at the National Institute of Standards and Technology (NIST) in Gaithersburg, Maryland, USA, and in 2015 he spend two months as a visiting researcher at University of California, Berkeley, USA. His research interest is in robotics, especially intelligent functions for mobile robots. Besides his work on mapping and SLAM, Dr. Schwertfeger is working on mobile manipulation and rescue robotics, object detection and robot autonomy. Sören Schwertfeger was the general chair of the 2017 IEEE International Symposium on Safety, Security, and Rescue Robotics (SSRR). He is a RoboCup Executive, an associate editor of the IEEE Robotics and Automation Magazine and recently published, as a guest editor, a special issue on SSRR in the Journal of Field Robotics.